Brain signaling becomes less integrated and more segregated with age

Rostam M Razban[a], Botond B Antal[b,e], Ken A Dill[a,d,f,*], and Lilianne R Mujica-Parodi[a,b,c,d,e,*]

[a]Laufer Center for Physical and Quantitative Biology, Stony Brook University, Stony Brook, NY, USA
[b]Dept. of Biomedical Engineering, Stony Brook University, Stony Brook, NY, USA
[c]Program in Neuroscience, Stony Brook University, Stony Brook, NY, USA
[d]Dept. of Physics and Astronomy, Stony Brook University, Stony Brook, NY, USA
[e]Athinoula A. Martinos Center for Biomedical Imaging, Massachusetts General Hospital and Harvard Medical School, Boston, MA, USA
[f]Dept. of Chemistry, Stony Brook University, Stony Brook, NY, USA
[*]correspondence dill@laufercenter.org, mujica@lcneuro.org

November 16, 2023

Abstract

The integration-segregation framework is a popular first step to understand brain dynamics because it simplifies brain dynamics into two states based on global vs. local signaling patterns. However, there is no consensus for how to best define what the two states look like. Here, we map integration and segregation to order and disorder states from the Ising model in physics to calculate state probabilities, P_{int} and P_{seg}, from functional MRI data. We find that integration/segregation decreases/increases with age across three databases, and changes are consistent with weakened connection strength among regions rather than topological connectivity based on structural and diffusion MRI data.

Keywords: network neuroscience | integration | segregation | aging | fMRI

Introduction

Aging is the number one risk factor for almost all neurodegenerative diseases [1]. For every 5 years after the age of 65, the probability of acquiring Alzheimer's disease doubles [2]. An influential conceptual approach to begin making sense of brain dynamics frames it in terms of a balance between *integrated* and *segregated* network states [3, 4, 5, 6, 7, 8]. On one hand, the brain faces functional pressure to have as many regions directly connected for quick communication. On the other hand, the brain is constrained to minimize metabolic energy consumption because it consumes ten-times more of the body's energy than expected by mass [9]. Tuning the balance between extensive global signaling, referred to as integration, and limited local signaling, referred to as segregation, optimally compromises between functional and energetic constraints [10, 11, 12, 13]. Although these constraints remain throughout life, aging disrupts their balance.

Previous research found mixed aging results, depending on the metrics used to measure integration and segregation [14, 15, 16, 17]. Although most in the literature use the system segregation metric [14], no consensus exists surrounding integration. In general, the problem facing the integration-segregation framework is that there is no one way to define the two states. Many graph theoretical metrics could potentially be used [18] and it is unclear why one should take precedence over the other, particularly when their aging outcomes are mutually inconsistent. There is a need to more fundamentally define integration and segregation to transform it from a proxy to a physical quantity.

Here, we provide a physical foundation for the framework by applying the mean field Ising model to treat integration and segregation as physical 2-phase systems like magnets and liquids. After demonstrating that the Ising model can capture global brain dynamics as measured by functional MRI once the effective number of nodes is properly set, we proceed to calculate probabilities of being in the integrated or segregated states and find that younger and older brains are bounded by optimal and random signaling, respectively. We then explore diffusion and structural MRI data to ask if the age-related changes in signaling are due to changes in topological network connectivity.

Applying the Ising model to fMRI

We model human brain signaling patterns obtained from data sets of resting-state functional MRI (fMRI). As in previous work [19], we capture those patterns using the Ising model, a widely used theoretical method for expressing macroscale behaviors in terms of interactions among many underlying microscale agents [20]. We first transform the continuous fMRI data into representation as discrete Ising spins via binarization of the data (Figure 1). That is, we reduce the state of the region as simply being negative or positive, following the way that Ising models have spins of either -1 or 1 (details in Methods). Second, we calculate the *synchrony* by summing over all spins in a given time interval and dividing by the total number of spins (Figure 1). Before proceeding to the last step of calculating the probability that the brain is in the segregated state P_{seg},[1] we first check whether the model so obtained can capture the experimental synchrony distributions.

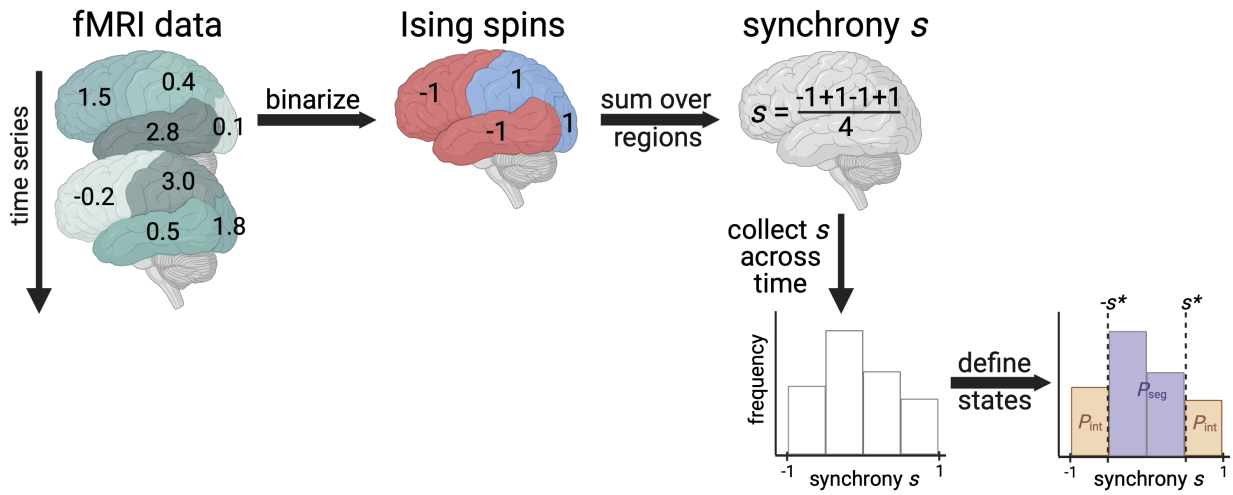

Figure 1: **Calculating the probability that the brain exhibits integrated or segregated dynamics (P_{int} or P_{seg}).** The schematic demonstrates the procedure for one individual's fictitious functional MRI scan with 4 brain regions and only two time points shown. First, we binarize data based on nearest neighbor scans in time. If functional MRI (fMRI) signal increases, a value of 1 is assigned; decreases, -1. Then, we calculate the average spin state of the brain, called synchrony. Finally, we collect synchrony values across the entire time series to create a synchrony distribution. We appropriately set the synchrony threshold based on Ising model theory to delineate between integrated and segregated microstates. Additional details can be found in the Methods. Figure created with Biorender.com.

[1] P_{int} trivially relates to P_{seg} because $P_{\text{int}} + P_{\text{seg}} = 1$.

Results

The number of functionally effective brain regions

An Ising model only considering pairwise interactions typically has one quantity of interest. The strength of connection λ between any two regions[2] corresponds to the degree to which signals between any two brain regions are correlated. However, we find that a naive fit of λ based on maximum entropy fails to capture the synchrony distribution from fMRI data (Figure 2, orange). To improve upon a standard Ising model approach, here we introduce a hyper-parameter N_{eff}. Brain atlas parcellations provide N brain regions, however, those N regions must be identically distributed across time for the Ising model to apply. We find that when setting N to a lower value N_{eff}, fixed for all individuals within a data set, the Ising model accurately captures synchrony distributions (Figure 2). The optimal value of $N_{\text{eff}} = 40$ is determined by scanning across N_{eff} multiples of 5 to find which best captures the next order moment not fit by our maximum entropy setup across all individuals (Methods, Figure 6). For our particular preprocessing (Methods), we find that $N_{\text{eff}} = 40$ for individuals in the Cambridge Center for Ageing (CamCAN) [21] and the Human Connectome Project Aging (HCP) [22]. For the UK Biobank (UKB) [23], $N_{\text{eff}} = 30$ performs best (Figure 6).

Based on identified N_{eff} hyper-parameter values, brains act as if they have a few tens of functional units. If different preprocessing decisions are considered, such as atlas resolution, N_{eff} values are still within an order of magnitude. At the voxel-level ($N = 125,879$), we obtain an N_{eff} value of 65 for CamCAN and 125 for HCP using the same procedure as for the Seitzman atlas ($N = 300$) considered in the previous paragraph (Figure S2). Future work will pinpoint how N_{eff} depends on preprocessing to enable a future study creating a physics-based parcellation of the brain.

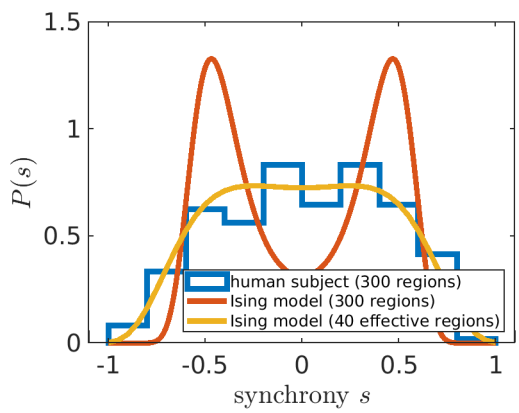

Figure 2: **Adjusting the number of brain regions (N_{eff}) helps capture experiment.** The modified Ising model with $N_{\text{eff}} = 40$ (yellow line) better captures the synchrony distribution (blue histogram) of an arbitrarily chosen individual in the Cambridge Centre for Ageing data set (subject id: CC110045). The orange line corresponds to the Ising model with N equal to the number of regions as in the Seitzman atlas [24], which is used in fMRI preprocessing.

The aging brain becomes functionally more segregated

P_{seg} is the relative number of time points for which the absolute value of synchrony is less than the delineating threshold between segregated and integrated microstates (Figure 1). The synchrony threshold s^* is set such that at the Ising model's critical point in connection strength λ, P_{seg} equals 1/2 for the ideal synchrony distribution based on Ising model theory (Methods). For CamCAN and HCP, $s^* = 0.33$ because $N_{\text{eff}} = 40$ for both data sets. For UKB, $s^* = 0.36$ (Table S1).

[2]Under standard Ising model notation, $\lambda = J/T$, where J corresponds to the coupling constant and T is the temperature of the bath.

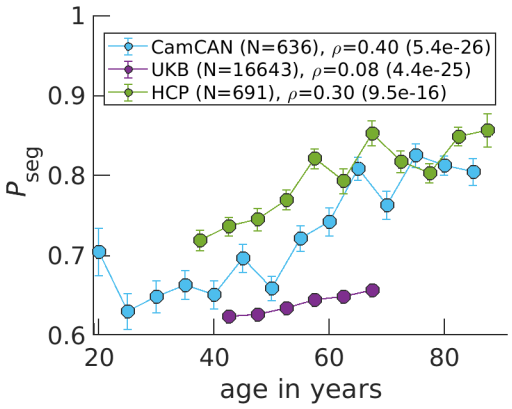

Figure 3: $P_{\mathbf{seg}}$ **rises in aging brains across three data sets.** Data points correspond to medians, while error bars correspond to standard errors for bins of 5 years. The variable ρ corresponds to the Spearman correlation coefficient between age and P_{seg} calculated over all N individuals, with the p-value in parenthesis.

Across the three publicly available data sets, we find that the balance shifts towards more segregation at older ages (Figure 3). Note that if we plotted P_{int} rather than P_{seg}, Figure 3 would be horizontally flipped, where P_{int} goes from high to low values as a function of increasing age because $P_{\text{seg}} + P_{\text{int}} = 1$. There is large variation among subjects (Figure S3). However, the correlation between age and P_{seg} is significant with the largest coefficient being 0.40 for CamCAN, while the lowest being 0.08 for UKB. Discrepancies in study designs may explain correlation magnitude differences: CamCAN and HCP are designed to study healthy aging [25, 26], while the goal of UKB is to identify early biomarkers for brain diseases [27].

Informed by the Ising model, increases in segregation result from network reorganization to more local signaling because of weakened connection strength between regions. Interestingly, younger individuals exhibit segregation behavior closer to the Ising model's critical point of connection strength (Figure S4). At the critical point, we define $P_{\text{seg}} = 1/2$ (Methods) and find experimental P_{seg} values closer to 1/2 for younger individuals (Figure 3). Older individuals, on the other hand, approach $P_{\text{seg}} = 1$ on average. This limit corresponds to functionally uncoupled brain regions that are randomly activating. Our results support the critical brain hypothesis that healthy brains operate near a critical point [28, 29, 30, 31] and implicate aging as pushing brain dynamics further away from criticality.

Changes in brain dynamics are not due to structural degradation

In the previous subsection, we discussed the disruption of the integration and segregation balance from the perspective of phase transitions in physics. Here, we explore the physiological mechanism underlying increasing segregation in the aging brain. We consecutively simulate the Ising model on a hypothetically degrading brain structure and show that random removal of edges yields qualitatively similar results to those of fMRI (Figure 4). Note that Figure 4 is horizontally flipped from those of P_{seg} (Figure 3) because average degree is on the x-axis. It is presumed that edges are lost as age increases. In Figure 4, edges are lost linearly in time, however, more complicated monotonic functions can be employed to yield a quantitative match with experimental data in Figure 3. We can also capture variability among individuals by assuming connection strengths within an individual are drawn from a distribution, rather than all being equal (Figure S6).

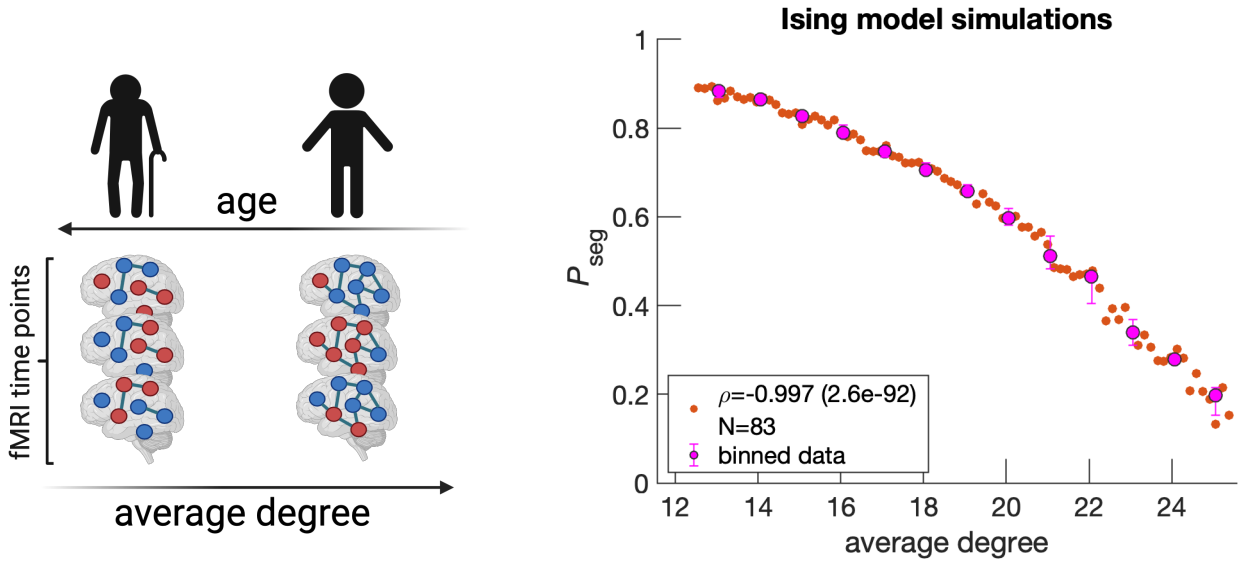

Figure 4: **Simulating the random removal of edges results in $P_{\mathbf{seg}}$ increases.** Five edges are randomly removed from a starting diffusion MRI structure (arbitrarily chosen UK Biobank individual, subject ID: 6025360). An Ising system is simulated and spin states, denoted by dark blue and red node colors, are recorded across 2500 time steps to calculate P_{seg}. Then, the entire procedure is repeated for the updated structure, for a total of 83 times (Methods). Orange data points on the right plot correspond to individual Ising systems, where N reflects the total number. The variable ρ corresponds to the Spearman correlation coefficient calculated over all orange data points between average degree and P_{seg}, with the p-value in parenthesis. Magenta data points correspond to medians, while error bars correspond to upper and lower quartiles for bin sizes of one degree. The schematic on the left is created with Biorender.com.

We now begin to investigate possible mechanisms of connection degradation. First, we find that our simulation is agnostic to the detailed mechanism of connection degeneration because connection strength is essentially modulated by the probability that a given edge exists (Figure S7). In other words, the simulation cannot inform whether connections are degraded based on some targeted property. Thus, we turn to MRI and diffusion MRI data from UKB to investigate possible properties being degraded with age. In Figure S8, we confirm that white matter volume decreases as a function of adult age, as previously reported [32, 33, 34]. However, this decrease does not correspond to a loss of anatomical connections because we find that neither average degree, average tract length nor average tract density monotonically decrease with age when analyzing diffusion MRI scans using the Q-Ball method (Figure S9). This seems to contradict previous findings which report decreases [35, 36]. However, previous results employed the more simple diffusion tension imaging (DTI) method which is known to be less accurate at performing tractography [37, 38, 39]. When rerunning our analysis for DTI, we can reproduce previously reported tract properties' anticorrelations with age (Figure S9).

We propose that the observed reduction in white matter volume (Figure S8) and brain dynamics changes corresponds to less myelin covering axons as function of age. Despite conclusively rejecting anatomical connections as a possible mechanism in the previous paragraph, it remains inconclusive whether myelin underlies trends because we are not aware of such data being publicly available. Although axons are still physically present, myelin coverage disruption causes regions to no longer be functionally connected because signals do not arrive on time. Previously reported results from Myelin Water Imaging confirm reduction in myelin at advanced ages [40, 41]. We also investigated whether degraded functional connections are likely to be longer than average with age, as previously reported for certain brain regions [42]. Although we indeed find that the average correlation of the 25% longest connections is slightly more strongly anticorrelated with age compared to the average correlation of the 25% shortest connections for CamCAN (Figure S10, left), we find the opposite trend for HCP (Figure S10, right). Thus, myelin reduction does not seem to have a stronger impact on longer connections and conclude that the loss of functional connections happens randomly with

respect to length at the brain-wide scale.

Discussion

We apply the mean field Ising model to physically quantify the integration and segregation framework at the emergent scale of the whole brain. From resting-state fMRI scans across three publicly available data sets, we find that brain dynamics steadily becomes more segregated with age. Physically, aging leads to brain dynamics moving further away from its optimal balance at the critical point. Physiologically, analyses of white matter properties point to random functional connection losses due to myelin degeneration as the possible culprit for more segregated dynamics.

The Ising model and integration-segregation frameworks are considered as the simplest approaches to capture dynamics in their respective fields. Thus, it is fitting to map segregated and integrated states in neuroscience to disordered and ordered Ising model phases in physics, respectively. One general challenge in applying graph theory to MRI-level data is identifying what constitutes a node [8, 43, 44, 45, 46, 47]. We identify the best number of effective brain regions N_{eff} such that the Ising model accurately captures individuals' synchrony distributions across the corresponding data set. Future work will utilize N_{eff} calculations to guide the creation of a parcellation in which brain regions are constrained to be physically independent based on their collective functional activity.

The field is inundated with integration and segregation metrics that have different aging trends. Our metric is mechanistically based on the connection strength between regions and stands out for two reasons. First, P_{seg} and P_{int} are naturally at the emergent scale of the brain. We do not calculate a local property and then average over nodes to yield a brain-wide value ([13] also has this strength). Second, P_{seg} and P_{int} are directly related because $P_{\text{seg}} + P_{\text{int}} = 1$. Most integration and segregation metrics [3, 18, 14, 13] are not defined to be anti-correlated[3].

Taken together, it is not surprising that P_{seg} and P_{int} results are not consistent with some previous reports. For example, a property called system segregation, defined as the difference between inter- and intra-correlations among modules, was found to decrease with age [14]. Although most report that segregation decreases with age, regardless of the specific metric [14, 48, 49, 17] (see [16] for an exception), integration trends are less clear. Global efficiency, taken from graph theory, was found to increase with age [14, 50]; however, others found different integration metrics decreasing with age [51, 52, 17], consistent with results reported here.

The utility of the integration-segregation framework lies in its simplicity. However, its simplicity has led to various heuristic definitions that have qualitatively different aging trends. By physically defining integration and segregation based on connection strength between regions, we provide an interpretable foundation for more detailed studies going beyond the two-state approximation to investigate brain dynamics.

Methods

fMRI preprocessing

We access three publicly available resting-state functional MRI data sets: Cambridge Centre for Ageing (CamCAN) [21], UK Biobank (UKB) [23], and Human Connectome Project (HCP) [22]. Acquisition details such as field strength and repetition time can be found in Table S2.

UKB and HCP fMRI data are accessed in preprocessed form (for details see [23] and [53, 54], respectively). We preprocessed CamCAN data as done in our previous work [19]. For all three data sets, the cleaned, voxel space time series are band-pass filtered to only include neuronal frequencies (0.01 to 0.1 Hz) and smoothed at a full width at half maximum of 5 mm. Finally, we parcellate into 300 regions of interest according to

[3] This can be advantageous because greater complexity can be captured [8].

the Seitzman atlas [24]. For our voxel-wide analysis presented in the Supporting Information, we do not parcellate and just consider gray mater voxels by masking.

Applying the Ising model requires data to only take two possible values: -1 or 1. After performing the preprocessing outlined in the previous paragraph, we binarize the continuous signal for a given region based on the sign of the slope of subsequent time points [19]. We previously showed that such binarization still yields similar time correlations as that of the originally continuous data [19].

Finally, we only consider brain scans that have the same number of measurements as the predominant number of individuals in the respective data set (Table S2). If the fitted connection strength parameter λ is less than 0, reflecting a nonphysical value, we do not include the individual's brain scan in our analysis. In the HCP dataset, we excluded individuals aged 90 years or older from our analyses because their exact age, considered protected health information, was not available.

Identifying the N_{eff} hyper-parameter

In Figure 2, our maximum entropy fit (orange line) fails to qualitatively capture the synchrony distribution for an arbitrary individual. To see if we can rescue the maximum entropy fit, we replace N with N_{eff} (Equation S1). In the right plot of Figure 5, we demonstrate that a fully connected Ising model with $N_{\text{eff}} = 40$ accurately captures the fourth moment of synchrony $\langle s^4 \rangle$ across all individuals in CamCAN, preprocessed under the Seitzman atlas. Note that N_{eff} is not a parameter like Λ; rather it is a hyper-parameter because it takes the same value across all individuals within the data set. N_{eff} is necessary because the Ising model systematically underestimates $\langle s^4 \rangle$ when $\Lambda > 0$ (left plot of Figure 5). Note that Λ corresponds to rescaling λ such that $\Lambda = 0$ is at the critical point (Equation S13).

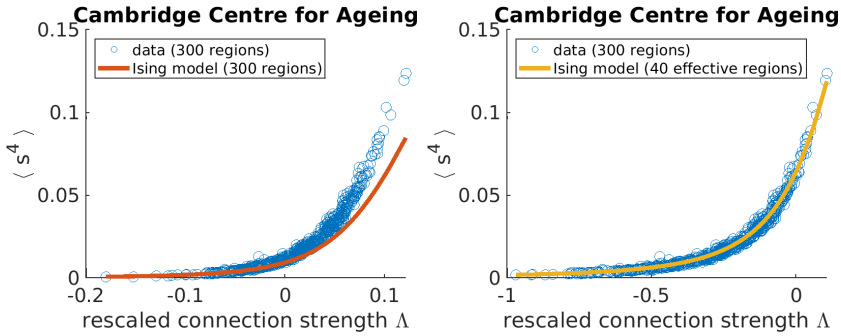

Figure 5: **Adjusting the effective number of brain regions (N_{eff}) helps capture synchrony distributions' variances across individuals in the Cambridge Centre for Ageing data set.** Each data point corresponds to an individual.

To identify $N_{\text{eff}} = 40$ as the best value, we perform a parameter scan over multiples of 5 and identify N_{eff} at which the root mean square error (RMSE) between $\langle s^4 \rangle_{\text{exp}}$ and $\langle s^4 \rangle_{\text{model}}$ is minimized (Figure 6). We choose the fourth moment because it is the next order moment that our maximum entropy fit does not constrain[4]. We could also use other metrics to identify N_{eff}, such as the Kullback-Leibler divergence.

[4]It is not the third moment because the distribution is assumed to be even as indicated by our prior (Equation S1).

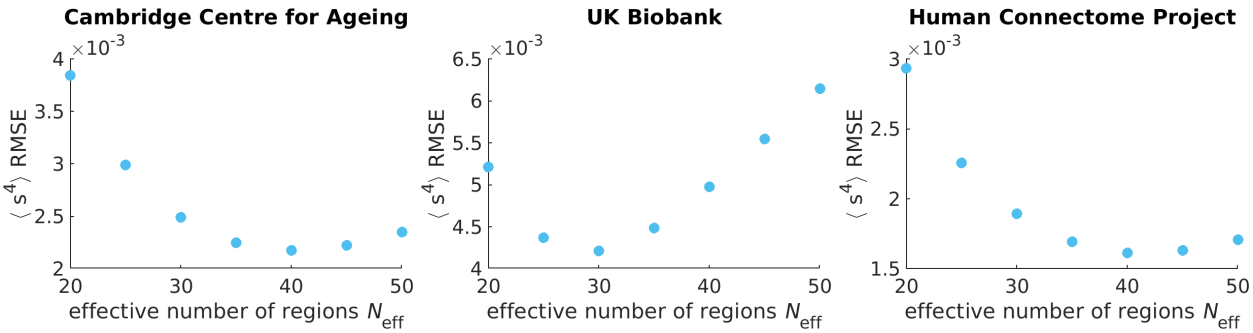

Figure 6: **The effective number of regions $N_{\mathbf{eff}}$ is identified by minimizing the root mean square error (RMSE) of the fourth moment of synchrony between theory and experiment across all individuals.** Each data point corresponds to the sum over all individuals' RMSEs in the respective data set.

Calculating $P_{\mathbf{seg}}$

The probability of the brain network being in the segregated state is the sum over all microstates corresponding to the segregated state.

$$P_{\text{seg}} = \frac{1}{Z} \sum_{n=-N_{\text{eff}}s^*}^{N_{\text{eff}}s^*} P(n) \tag{1}$$

$$P_{\text{seg}} = \frac{1}{Z} \sum_{n=-N_{\text{eff}}s^*}^{N_{\text{eff}}s^*} \binom{N_{\text{eff}}}{(N_{\text{eff}}+n)/2} e^{\lambda n^2/N_{\text{eff}}^2} \tag{2}$$

In the second line, the expression for $P(n)$ is the solution to the mean field Ising model (Equation S3). The constant s^* is the synchrony threshold for which segregated and integrated microstates are delineated. We set s^* such that $P_{\text{seg}} = 1/2$ when $\Lambda = 0$ according to theory. More specifically, we numerically calculate $P_{\text{seg}}(\Lambda = 0)$ for a given N_{eff} and extrapolate to find s^* (Figure S5). Proper calibration ensures that the theory is accurate and enables apples to apples P_{seg} comparisons across data sets with different N_{eff}. The list of s^* values for the three publicly available data sets studied can be found in Table S1.

Ising model simulation

We simulate the Ising model on an initial structure informed by diffusion MRI under the Harvard-Oxford atlas [55] (64 regions) for an arbitrarily chosen UK Biobank individual (subject ID: 6025360). Edge removal procedures all begin with this starting structure. If no edge exists between two regions, then the regions are uncoupled. If an edge does exist, then regions i and j are coupled and contribute $\lambda * \sigma_i * \sigma_j$ to the system's energy; where λ corresponds to the connection strength and σ corresponds to the spin state of the corresponding region (-1 or 1). λ is set to 0.0084, which is above its critical point (starting $P_{\text{seg}} \approx 0.2$).

The simulation for a given structure starts by randomly assigning the 64 nodes up or down spins. Then, for each time step, we attempt 10 spin flips 64 times for a total of 2500 time steps. Spin flips are accepted according to the Metropolis-Hastings algorithm [56]. The exact number of spin flip attempts or total time points does not matter, as long as equilibrium is reached. For example, we find that for λ values larger than those presented in the text, synchrony distributions become asymmetric and exhibit only one of the two peaks corresponding to the integrated state because of the high kinetic barrier of going from all down spins to all up spins.

Although the starting structure is informed by diffusion MRI, resulting structures after edge removals are based on the posited removal strategy. Edges informed by dMRI are undirected and removal maintains undirectedness. Effectively two times as many edges are removed because both forward and backward edges are concurrently eliminated.

Diffusion MRI analysis

Diffusion MRI processing to obtain structural information like tract length and streamline count, which we call tract density, are outlined in our previous work [57]. Briefly, we take preprocessed dMRI scans from the UK Biobank [27] and calculate connectivity matrices using the Diffusion Imaging in Python software [39]. We input the Talairach atlas [58] to distinguish between white and gray matter. We perform deterministic tractography and reconstruct the orientation distribution function using Constant Solid Angle (Q-Ball) with a spherical harmonic order of 6 [59]. For Figure S9, we also do reconstruction using diffusion tensor imaging [39]. To generate the starting structure for Ising model simulations, we input the Harvard-Oxford atlas for tractography because it parcellates the brain into a fewer number of regions, making it more computationally tractable to carry out simulations.

Code and data availability

Scripts necessary to reproduce figures and conclusions reached in the text can be found at github.com/rrazban/2state_brain. Please refer to the respective publicly available diffusion MRI data set to access previously published data (CamCAN, UKB and HCP) [21, 22, 23].

Acknowledgments

We thank Ying-Jen Yang, Anthony Chesebro, Charles Kocher, Jonathan Pachter and Lakshman Verma for insightful discussions. The research described in this paper is funded by the White House Brain Research Through Advancing Innovative Technologies (BRAIN) Initiative (NSFNCS-FR 1926781 to L.R.M.-P. and K.A.D.) and the Stony Brook University Laufer Center for Physical and Quantitative Biology (K.A.D.).

Data collection and sharing for this project was provided by the Cambridge Centre for Ageing and Neuroscience (CamCAN). CamCAN funding was provided by the UK Biotechnology and Biological Sciences Research Council (grant number BB/H008217/1), together with support from the UK Medical Research Council and University of Cambridge, UK.

This research has been conducted using the UK Biobank Resource under Application Number 37462.

Research reported in this publication was supported by the National Institute On Aging of the National Institutes of Health under Award Number U01AG052564 and by funds provided by the McDonnell Center for Systems Neuroscience at Washington University in St. Louis. The HCP-Aging 2.0 Release data used in this report came from DOI: 10.15154/1520707.

Supporting Information

Deriving the Ising model with N_{eff}

Many have derived the probability distribution of the mean field Ising model, otherwise known as the fully connected or Curie-Weiss Ising model [19, 60, 61]. Here, we demonstrate how to introduce N_{eff} in a Maximum Entropy framework. The tricky part is that N_{eff} defines the state space over which the probability distribution is summed.

Adding a global pairwise correlation constraint, we obtain the following Lagrangian function over the net displacement of spin states $n = \sum_i^{N_{\text{eff}}} \sigma_i$, where σ_i can take a value of 1 or -1.

$$\mathcal{L} = \sum_n^{N_{\text{eff}}} P(n) \ln \frac{P(n)}{q(n)} + \alpha \left(\sum_n^{N_{\text{eff}}} P(n) - 1 \right) + \lambda \left(\frac{1}{(N_{\text{eff}})^2} \sum_n^{N_{\text{eff}}} n^2 P(n) - \langle s^2 \rangle_{\text{exp}} \right) \tag{S1}$$

P is the probability distribution. q corresponds to the prior and is set to the binomial distribution $\binom{N}{(N+n)/2} 2^{-N}$, where the binomial coefficient captures the number of ways individual spins can organize for a given n. α and λ correspond to the Lagrange multipliers that enforce the constraints that the probability

distribution is normalized and the mean pairwise correlation equals $\langle s^2 \rangle$, respectively. The variable s corresponds to the synchrony[5] and is limited to vary from -1 to 1 because $n = N_{\text{eff}} s$. This is the reason N does not have to be the same for $\langle s^2 \rangle_{\text{exp}}$ and $\langle s^2 \rangle_{\text{model}}$; $\langle s^2 \rangle$ is always bounded between -1 to 1.

Maximizing the Lagrangian function (Equation S1) with respect to P, we obtain the following distribution:

$$P(n) = Z^{-1} \binom{N_{\text{eff}}}{(N_{\text{eff}} + n)/2} e^{\lambda n^2 / N_{\text{eff}}^2} \tag{S2}$$

$$P(s) = Z^{-1} \binom{N_{\text{eff}}}{N_{\text{eff}}(1+s)/2} e^{\lambda s^2} \tag{S3}$$

Z corresponds to the partition function and ensures that P is normalized. Note that Z subsumes the α Lagrange multiplier.

Ising model phase transitions

The Landau model is a general formulation to study phase transitions [62, 20]. It takes the following form,

$$F(T) = A(T - T_c)\eta^2 + B\eta^4 \tag{S4}$$

η corresponds to the order parameter. F is the free energy and can be expressed as the probability for being in microstate i by the following relationship $F_i = k_b T \ln P_i$. T is the temperature and T_c corresponds to the critical temperature at which a second-order phase transition occurs. A and B are constants.

Here, we will express the Ising model (Equation S3) in terms of the Landau formalism (Equation S4) by approximating the binomial coefficient as an exponential to $\mathcal{O}(s^4)$. For brevity, we will write N to represent N_{eff}. First, we use Stirling's approximation to expand the binomial coefficient.

$$\binom{N}{N(1+s)/2} = N! \left[(N(1+s)/2)! \, (N(1-s)/2)! \right]^{-1} \tag{S5}$$

$$\approx N^N \left[\left(\frac{N(1+s)}{2} \right)^{\frac{N(1+s)}{2}} \left(\frac{N(1-s)}{2} \right)^{\frac{N(1-s)}{2}} \right]^{-1} \tag{S6}$$

$$= N^N \left[\left(\frac{N}{2} \right)^{\frac{N(1+s)}{2}} (1+s)^{\frac{N(1+s)}{2}} \left(\frac{N}{2} \right)^{\frac{N(1-s)}{2}} (1-s)^{\frac{N(1-s)}{2}} \right]^{-1} \tag{S7}$$

$$= N^N \left[\left(\frac{N}{2} \right)^N ([1+s][1-s])^{N/2} \left(\frac{1+s}{1-s} \right)^{Ns/2} \right]^{-1} \tag{S8}$$

$$= 2^N \left[\frac{1}{1-s^2} \left(\frac{1-s}{1+s} \right)^s \right]^{N/2} \tag{S9}$$

To make further headway, we assume $s \approx 0$ and expand Equation S9 to order s^4.

$$\binom{N}{N(1+s)/2} \approx 2^N \left[1 - s^2 - \frac{1}{3} s^4 \right]^{N/2} \tag{S10}$$

Next, we assume N is large and express the term under the brackets as an exponential.

[5] In ferromagnetic applications, s is commonly referred to as the magnetization.

$$\binom{N}{N(1+s)/2} \approx 2^N \exp\left[-\frac{N}{2}s^2 - \frac{N}{12}s^4\right] \tag{S11}$$

We can insert our approximate expression for the binomial coefficient back into $P(s)$ (Equation S3) and obtain,

$$P(s) \approx Z^{-1}2^N \exp\left[\left(\lambda - \frac{N}{2}\right)s^2 - \frac{N}{12}s^4\right] \tag{S12}$$

Note that Equation S12 (after transforming into free energy space) maps onto Landau theory (Equation S4). s corresponds to the order parameter and $\lambda_c = N/2$. At $\lambda = \lambda_c$, $P(s)$ switches from unimodal to bimodal, corresponding to a second order phase transition. We report a rescaled version of λ called Λ in Figure S4 and in other places in the Supporting Information to easily gauge how far an individual's connection strength is from the critical point.

$$\Lambda = \frac{\lambda - \lambda_{\text{critical}}}{\lambda_{\text{critical}}} \tag{S13}$$

Alternative N_{eff} fitting approach

Rather than choose one N_{eff} for all individuals in the data set as done in the main text, we could fit N_{eff} for each individual. Figure S1 demonstrates that such a procedure results in N_{eff} values that are highly linearly correlated with λ. In other words, more precise N_{eff} fits do not provide any more insight than maximum entropy fits of λ for all individuals in a data set under one optimal N_{eff}.

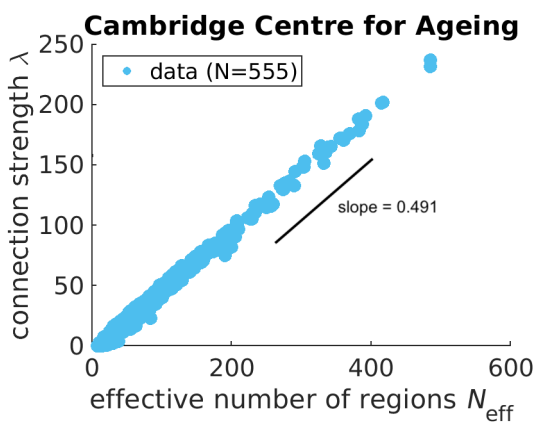

Figure S1: Treating N_{eff} as a parameter and fitting it per individual yields a strong correlation with λ. Each point reflects an individual brain scan and N reflects the total number analyzed. The value of the slope corresponds to that of the best-fit line for the data.

The N_{eff}-λ relationship can be reasoned from the analytical expression for $P(s)$ (Equation S12). When $\Lambda < 0$, which many individuals satisfy (Figure S4), $P(s)$ is well-approximated as a Gaussian.

$$P(s) \propto \exp\left[\left(\lambda - \frac{N_{\text{eff}}}{2}\right)s^2\right] \tag{S14}$$

Thus, the analytical form for $\langle s^2 \rangle$ is:

$$\langle s^2 \rangle = -\frac{1}{2\lambda - N_{\text{eff}}} \tag{S15}$$

Since λ is fit in the Maximum Entropy framework to exactly match $\langle s^2 \rangle$, Equation S15 indicates that a larger N_{eff} requires a larger λ for a fixed $\langle s^2 \rangle$. Indeed, we find in Figure S1 that the best fit line of the N_{eff}-λ relationship has an approximate slope of 0.5, in agreement with Equation S15.

Miscellaneous

Additional supplementary tables and figures that are directly referenced in the main text. For Figures presenting data set results, we adopt the following symbol codes unless otherwise noted. Data points correspond to individuals, where N reflects the total number. The variable ρ corresponds to the Spearman correlation coefficient between age and the property of interest (i.e. P_{seg}, white matter volume) calculated over all individuals, with the p-value in parenthesis. Error bars correspond to standard errors for equally spaced bins.

Table S1: Data set values for P_{seg} calculation.

Data set	effective number of regions N_{eff}	synchrony threshold s^*
Cambridge Centre for Ageing	40	0.334
UK Biobank	30	0.357
Human Connectome Project	40	0.334

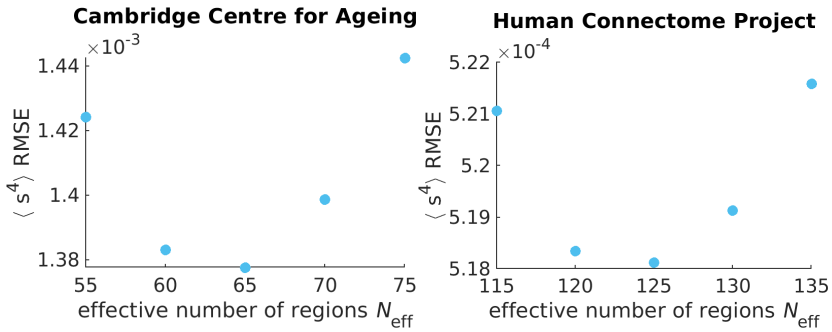

Figure S2: Identifying the effective number of regions N_{eff} for brain scans preprocessed at the voxel-level. Each data point corresponds to the sum over all individuals' RMSEs in the respective data set.

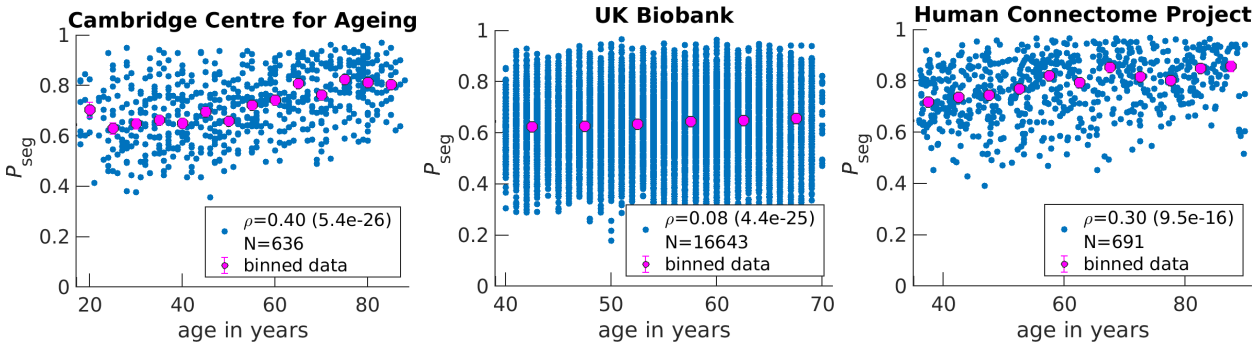

Figure S3: P_{seg} rises in aging brains across three data sets. Blue data points correspond to individuals, where N reflects the total number. The variable ρ corresponds to the Spearman correlation coefficient between age and P_{seg} calculated over all individuals, with the p-value in parenthesis. Magenta data points correspond to medians, while error bars correspond to standard errors for bins of 5 years.

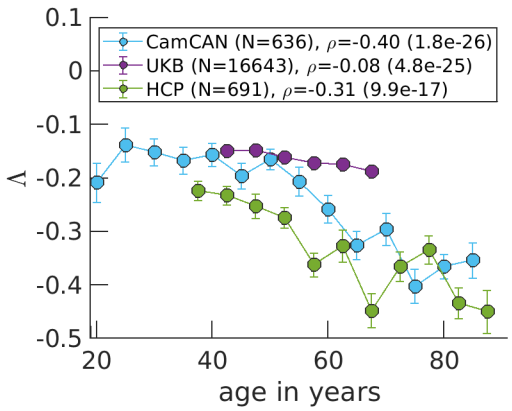

Figure S4: The rescaled connection strength parameter Λ moves further away from the critical point ($\Lambda = 0$) as age increases. Trends are similar in form to Figure 3 because P_{seg} is a function of Λ.

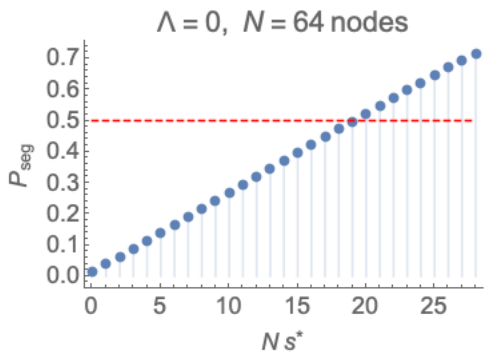

Figure S5: The synchrony threshold s^* is chosen such that it delineates between integrated and segregated states when $P_{\text{seg}} = P_{\text{int}} = 1/2$ (red line) at the critical point ($\Lambda = 0$). This particular figure is created for 64 nodes; it must be set to the corresponding data set's N_{eff} to determine the appropriate synchrony threshold.

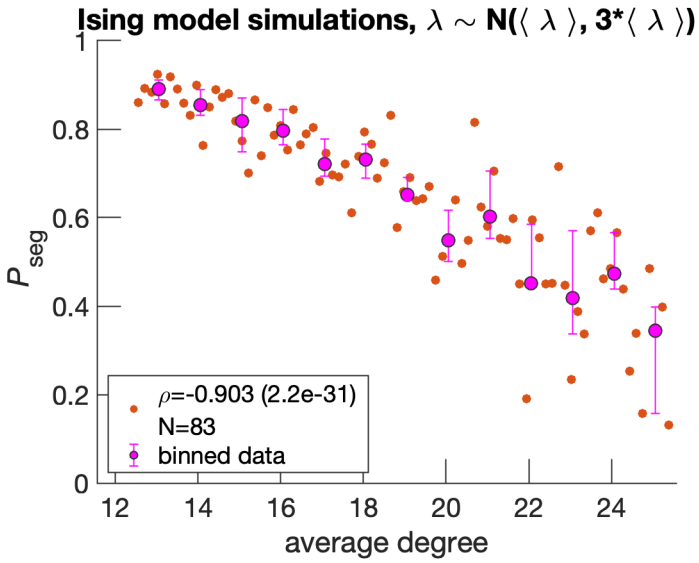

Figure S6: Greater variance in simulations is seen when edges' connection strengths λ are drawn from a normal distribution with mean $\langle\lambda\rangle$ and standard deviation $3 * \langle\lambda\rangle$. At each consecutive step, $\langle\lambda\rangle$ is attenuated such that 5 edges are removed per step from the same starting dMRI structure as in Figure 4 ($\langle\lambda'\rangle = \langle\lambda\rangle p_{\text{edge}}$).

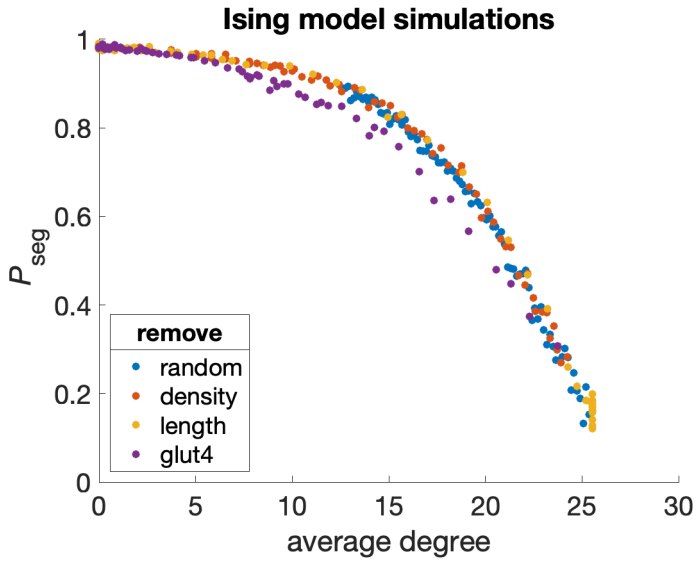

Figure S7: Edge removal mechanisms only matter in so much as they attenuate average degree. In addition to randomly removing edges as shown in Figure 4, we remove edges based on targeted attack of tract density, tract length, and a node's GLUT4 receptor density. Edges are removed in sequential order, such that those with the largest value are removed first. For all properties except for random, we remove edges until none are present.

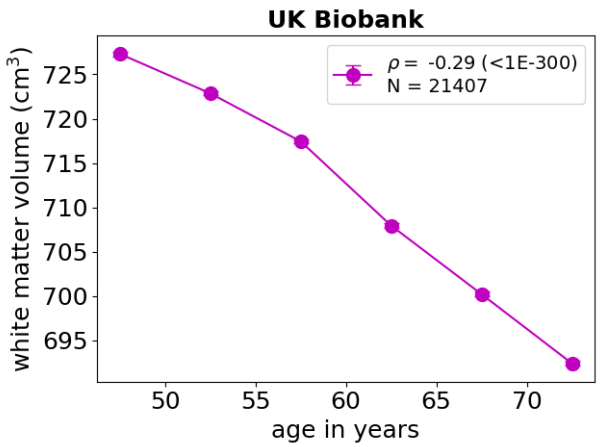

Figure S8: White matter volume decreases with age. White matter volume is measured by structural MRI provided by the UK Biobank. Error bars that represent standard errors are plotted but are not visible because of their minuscule size.

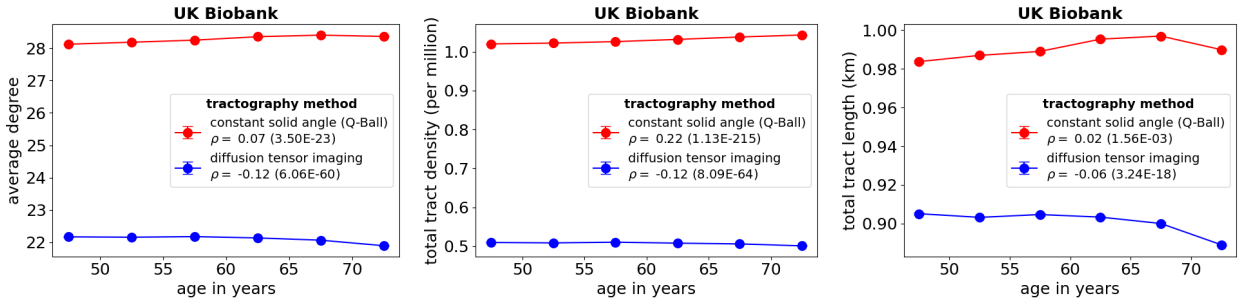

Figure S9: White matter tract properties do not degrade as a function of age when using the Q-Ball method for tractography. However, they do degrade with age when using the less accurate diffusion tensor imaging method. Error bars that represent standard errors are plotted but are not visible because of their minuscule size.

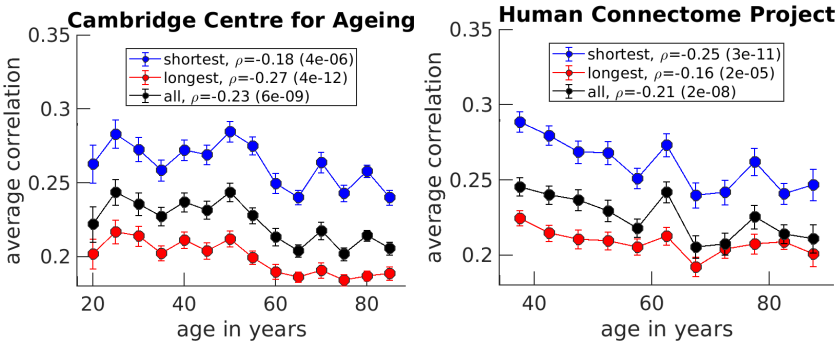

Figure S10: For the Cambridge Centre for Ageing data set, the shortest edges (lower quartile) have average Pearson correlations which correlate weaker than those of the longest edges (upper quartile). For the Human Connectome project, the opposite is the case. Edge distances are measured by center of mass coordinates of the brain regions based on the Seitzman atlas. Shortest and longest edges correspond to the lower and upper quartile (25%), respectively. Only positive correlations are considered and diagonal elements are ignored.

Table S2: Functional MRI acquisition parameters of the data sets.

Data set	field strength	repetition time	echo time	flip angle	voxel size	total time points
CamCAN	3T	1970 ms	30 ms	78°	3x3x4.44 mm^3	241
UK Biobank	3T	735 ms	39 ms	52°	2.4x2.4x2.4 mm^3	490
HCP	3T	800 ms	37 ms	52°	2x2x2 mm^3	1912

References

[1] Brian K Kennedy, Shelley L Berger, Anne Brunet, Judith Campisi, Ana Maria Cuervo, Elissa S Epel, Claudio Franceschi, Gordon J Lithgow, Richard I Morimoto, Jeffrey E Pessin, et al. Geroscience: linking aging to chronic disease. *Cell*, 159(4):709–713, 2014.

[2] F Bermejo-Pareja, J Benito-León, S Vega, MJ Medrano, Gustavo C Roman, Neurological Disorders in Central Spain (NEDICES) Study Group, et al. Incidence and subtypes of dementia in three elderly populations of central spain. *Journal of the neurological sciences*, 264(1-2):63–72, 2008.

[3] Giulio Tononi, Olaf Sporns, and Gerald M Edelman. A measure for brain complexity: relating functional segregation and integration in the nervous system. *Proceedings of the National Academy of Sciences*, 91(11):5033–5037, 1994.

[4] Olaf Sporns. Network attributes for segregation and integration in the human brain. *Current opinion in neurobiology*, 23(2):162–171, 2013.

[5] Gustavo Deco, Giulio Tononi, Melanie Boly, and Morten L Kringelbach. Rethinking segregation and integration: contributions of whole-brain modelling. *Nature Reviews Neuroscience*, 16(7):430–439, 2015.

[6] Gagan S Wig. Segregated systems of human brain networks. *Trends in cognitive sciences*, 21(12):981–996, 2017.

[7] Karl J Friston. Modalities, modes, and models in functional neuroimaging. *Science*, 326(5951):399–403, 2009.

[8] Olaf Sporns. *Networks of the Brain*. MIT press, 2010.

[9] Marcus E Raichle. The brain's dark energy. *Science*, 314(5803):1249–1250, 2006.

[10] Ed Bullmore and Olaf Sporns. The economy of brain network organization. *Nature reviews neuroscience*, 13(5):336–349, 2012.

[11] Peter Manza, Corinde E Wiers, Ehsan Shokri-Kojori, Danielle Kroll, Dana Feldman, Melanie Schwandt, Gene-Jack Wang, Dardo Tomasi, and Nora D Volkow. Brain network segregation and glucose energy utilization: relevance for age-related differences in cognitive function. *Cerebral Cortex*, 30(11):5930–5942, 2020.

[12] Jessica R Cohen and Mark D'Esposito. The segregation and integration of distinct brain networks and their relationship to cognition. *Journal of Neuroscience*, 36(48):12083–12094, 2016.

[13] Rong Wang, Mianxin Liu, Xinhong Cheng, Ying Wu, Andrea Hildebrandt, and Changsong Zhou. Segregation, integration, and balance of large-scale resting brain networks configure different cognitive abilities. *Proceedings of the National Academy of Sciences*, 118(23):e2022288118, 2021.

[14] Micaela Y Chan, Denise C Park, Neil K Savalia, Steven E Petersen, and Gagan S Wig. Decreased segregation of brain systems across the healthy adult lifespan. *Proceedings of the National Academy of Sciences*, 111(46):E4997–E5006, 2014.

[15] Keiichi Onoda and Shuhei Yamaguchi. Small-worldness and modularity of the resting-state functional brain network decrease with aging. *Neuroscience letters*, 556:104–108, 2013.

[16] Xue Chen, Joe Necus, Luis R Peraza, Ramtin Mehraram, Yanjiang Wang, John T O'Brien, Andrew Blamire, Marcus Kaiser, and John-Paul Taylor. The functional brain favours segregated modular connectivity at old age unless affected by neurodegeneration. *Communications biology*, 4(1):973, 2021.

[17] Yinghui Zhang, Yin Wang, Nan Chen, Man Guo, Xiuzhen Wang, Guangcai Chen, Yongchao Li, Lin Yang, Shan Li, Zhijun Yao, et al. Age-associated differences of modules and hubs in brain functional networks. *Frontiers in aging neuroscience*, 12:607445, 2021.

[18] Mikail Rubinov and Olaf Sporns. Complex network measures of brain connectivity: uses and interpretations. *Neuroimage*, 52(3):1059–1069, 2010.

[19] Corey Weistuch, Lilianne R Mujica-Parodi, Rostam M Razban, Botond Antal, Helena van Nieuwenhuizen, Anar Amgalan, and Ken A Dill. Metabolism modulates network synchrony in the aging brain. *Proceedings of the national academy of sciences*, 118(40):e2025727118, 2021.

[20] Ken Dill and Sarina Bromberg. *Molecular driving forces: statistical thermodynamics in biology, chemistry, physics, and nanoscience*. Garland Science, 2012.

[21] Jason R Taylor, Nitin Williams, Rhodri Cusack, Tibor Auer, Meredith A Shafto, Marie Dixon, Lorraine K Tyler, Richard N Henson, et al. The cambridge centre for ageing and neuroscience (cam-can) data repository: Structural and functional mri, meg, and cognitive data from a cross-sectional adult lifespan sample. *Neuroimage*, 144:262–269, 2017.

[22] Michael P Harms, Leah H Somerville, Beau M Ances, Jesper Andersson, Deanna M Barch, Matteo Bastiani, Susan Y Bookheimer, Timothy B Brown, Randy L Buckner, Gregory C Burgess, et al. Extending the human connectome project across ages: Imaging protocols for the lifespan development and aging projects. *Neuroimage*, 183:972–984, 2018.

[23] Fidel Alfaro-Almagro, Mark Jenkinson, Neal K Bangerter, Jesper LR Andersson, Ludovica Griffanti, Gwenaëlle Douaud, Stamatios N Sotiropoulos, Saad Jbabdi, Moises Hernandez-Fernandez, Emmanuel Vallee, et al. Image processing and quality control for the first 10,000 brain imaging datasets from uk biobank. *Neuroimage*, 166:400–424, 2018.

[24] Benjamin A Seitzman, Caterina Gratton, Scott Marek, Ryan V Raut, Nico UF Dosenbach, Bradley L Schlaggar, Steven E Petersen, and Deanna J Greene. A set of functionally-defined brain regions with improved representation of the subcortex and cerebellum. *Neuroimage*, 206:116290, 2020.

[25] Meredith A Shafto, Lorraine K Tyler, Marie Dixon, Jason R Taylor, James B Rowe, Rhodri Cusack, Andrew J Calder, William D Marslen-Wilson, John Duncan, Tim Dalgleish, et al. The cambridge centre for ageing and neuroscience (cam-can) study protocol: a cross-sectional, lifespan, multidisciplinary examination of healthy cognitive ageing. *BMC neurology*, 14:1–25, 2014.

[26] Susan Y Bookheimer, David H Salat, Melissa Terpstra, Beau M Ances, Deanna M Barch, Randy L Buckner, Gregory C Burgess, Sandra W Curtiss, Mirella Diaz-Santos, Jennifer Stine Elam, et al. The lifespan human connectome project in aging: an overview. *Neuroimage*, 185:335–348, 2019.

[27] Cathie Sudlow, John Gallacher, Naomi Allen, Valerie Beral, Paul Burton, John Danesh, Paul Downey, Paul Elliott, Jane Green, Martin Landray, et al. Uk biobank: an open access resource for identifying the causes of a wide range of complex diseases of middle and old age. *PLoS medicine*, 12(3):e1001779, 2015.

[28] John M Beggs and Dietmar Plenz. Neuronal avalanches in neocortical circuits. *Journal of neuroscience*, 23(35):11167–11177, 2003.

[29] Enzo Tagliazucchi, Pablo Balenzuela, Daniel Fraiman, and Dante R Chialvo. Criticality in large-scale brain fmri dynamics unveiled by a novel point process analysis. *Frontiers in physiology*, 3:15, 2012.

[30] John M Beggs. Addressing skepticism of the critical brain hypothesis. *Frontiers in Computational Neuroscience*, 16, 2022.

[31] Adrián Ponce-Alvarez, Morten L Kringelbach, and Gustavo Deco. Critical scaling of whole-brain resting-state dynamics. *Communications Biology*, 6(1):627, 2023.

[32] Catherine Lebel, Myrlene Gee, Richard Camicioli, Marguerite Wieler, Wayne Martin, and Christian Beaulieu. Diffusion tensor imaging of white matter tract evolution over the lifespan. *Neuroimage*, 60(1):340–352, 2012.

[33] Richard AI Bethlehem, Jakob Seidlitz, Simon R White, Jacob W Vogel, Kevin M Anderson, Chris Adamson, Sophie Adler, George S Alexopoulos, Evdokia Anagnostou, Ariosky Areces-Gonzalez, et al. Brain charts for the human lifespan. *Nature*, 604(7906):525–533, 2022.

[34] Katherine E Lawrence, Leila Nabulsi, Vigneshwaran Santhalingam, Zvart Abaryan, Julio E Villalon-Reina, Talia M Nir, Iyad Ba Gari, Alyssa H Zhu, Elizabeth Haddad, Alexandra M Muir, et al. Age and sex effects on advanced white matter microstructure measures in 15,628 older adults: a uk biobank study. *Brain Imaging and Behavior*, 15(6):2813–2823, 2021.

[35] Richard F Betzel, Lisa Byrge, Ye He, Joaquín Goñi, Xi-Nian Zuo, and Olaf Sporns. Changes in structural and functional connectivity among resting-state networks across the human lifespan. *Neuroimage*, 102:345–357, 2014.

[36] Sol Lim, Cheol E Han, Peter J Uhlhaas, and Marcus Kaiser. Preferential detachment during human brain development: age-and sex-specific structural connectivity in diffusion tensor imaging (dti) data. *Cerebral Cortex*, 25(6):1477–1489, 2015.

[37] Derek K Jones, Thomas R Knösche, and Robert Turner. White matter integrity, fiber count, and other fallacies: the do's and don'ts of diffusion mri. *Neuroimage*, 73:239–254, 2013.

[38] Ariel Rokem, Jason D Yeatman, Franco Pestilli, Kendrick N Kay, Aviv Mezer, Stefan Van Der Walt, and Brian A Wandell. Evaluating the accuracy of diffusion mri models in white matter. *PloS one*, 10(4):e0123272, 2015.

[39] Eleftherios Garyfallidis, Matthew Brett, Bagrat Amirbekian, Ariel Rokem, Stefan Van Der Walt, Maxime Descoteaux, Ian Nimmo-Smith, and Dipy Contributors. Dipy, a library for the analysis of diffusion mri data. *Frontiers in neuroinformatics*, 8:8, 2014.

[40] Muzamil Arshad, Jeffrey A Stanley, and Naftali Raz. Adult age differences in subcortical myelin content are consistent with protracted myelination and unrelated to diffusion tensor imaging indices. *Neuroimage*, 143:26–39, 2016.

[41] Irina S Buyanova and Marie Arsalidou. Cerebral white matter myelination and relations to age, gender, and cognition: A selective review. *Frontiers in human neuroscience*, 15:662031, 2021.

[42] Dardo Tomasi and Nora D Volkow. Aging and functional brain networks. *Molecular psychiatry*, 17(5):549–558, 2012.

[43] BT Thomas Yeo and Simon B Eickhoff. A modern map of the human cerebral cortex. *Nature*, 536(7615):152–154, 2016.

[44] Gagan S Wig, Bradley L Schlaggar, and Steven E Petersen. Concepts and principles in the analysis of brain networks. *Annals of the New York Academy of Sciences*, 1224(1):126–146, 2011.

[45] Javier DeFelipe. From the connectome to the synaptome: an epic love story. *science*, 330(6008):1198–1201, 2010.

[46] Sebastian Seung. *Connectome: How the brain's wiring makes us who we are*. HMH, 2012.

[47] Thomas Charles Lacy and Peter A Robinson. Effects of parcellation and threshold on brainconnectivity measures. *Plos one*, 15(10):e0239717, 2020.

[48] Bradley R King, Peter Van Ruitenbeek, Inge Leunissen, Koen Cuypers, K-F Heise, Thiago Santos Monteiro, Lize Hermans, Oron Levin, Genevieve Albouy, Dante Mantini, et al. Age-related declines in motor performance are associated with decreased segregation of large-scale resting state brain networks. *Cerebral Cortex*, 28(12):4390–4402, 2018.

[49] Jessica S Damoiseaux. Effects of aging on functional and structural brain connectivity. *Neuroimage*, 160:32–40, 2017.

[50] Zhijun Yao, Ying Zou, Weihao Zheng, Zhe Zhang, Yuan Li, Yue Yu, Zicheng Zhang, Yu Fu, Jie Shi, Wenwen Zhang, et al. Structural alterations of the brain preceded functional alterations in major depressive disorder patients: Evidence from multimodal connectivity. *Journal of affective disorders*, 253:107–117, 2019.

[51] Joanna Su Xian Chong, Kwun Kei Ng, Jesisca Tandi, Chenhao Wang, Jia-Hou Poh, June C Lo, Michael WL Chee, and Juan Helen Zhou. Longitudinal changes in the cerebral cortex functional organization of healthy elderly. *Journal of Neuroscience*, 39(28):5534–5550, 2019.

[52] Meike Oschmann, Jodie R Gawryluk, and Alzheimer's Disease Neuroimaging Initiative. A longitudinal study of changes in resting-state functional magnetic resonance imaging functional connectivity networks during healthy aging. *Brain Connectivity*, 10(7):377–384, 2020.

[53] Matthew F Glasser, Stamatios N Sotiropoulos, J Anthony Wilson, Timothy S Coalson, Bruce Fischl, Jesper L Andersson, Junqian Xu, Saad Jbabdi, Matthew Webster, Jonathan R Polimeni, et al. The minimal preprocessing pipelines for the human connectome project. *Neuroimage*, 80:105–124, 2013.

[54] Matthew F Glasser, Timothy S Coalson, Janine D Bijsterbosch, Samuel J Harrison, Michael P Harms, Alan Anticevic, David C Van Essen, and Stephen M Smith. Using temporal ica to selectively remove global noise while preserving global signal in functional mri data. *Neuroimage*, 181:692–717, 2018.

[55] Nikos Makris, Jill M Goldstein, David Kennedy, Steven M Hodge, Verne S Caviness, Stephen V Faraone, Ming T Tsuang, and Larry J Seidman. Decreased volume of left and total anterior insular lobule in schizophrenia. *Schizophrenia research*, 83(2-3):155–171, 2006.

[56] Nicholas Metropolis, Arianna W Rosenbluth, Marshall N Rosenbluth, Augusta H Teller, and Edward Teller. Equation of state calculations by fast computing machines. *The journal of chemical physics*, 21(6):1087–1092, 1953.

[57] Rostam M Razban, Jonathan Asher Pachter, Ken A Dill, and Lilianne R Mujica-Parodi. Early path dominance as a principle for neurodevelopment. *Proceedings of the National Academy of Sciences*, 120(16):e2218007120, 2023.

[58] Jack L Lancaster, Marty G Woldorff, Lawrence M Parsons, Mario Liotti, Catarina S Freitas, Lacy Rainey, Peter V Kochunov, Dan Nickerson, Shawn A Mikiten, and Peter T Fox. Automated talairach atlas labels for functional brain mapping. *Human brain mapping*, 10(3):120–131, 2000.

[59] Iman Aganj, Christophe Lenglet, Guillermo Sapiro, Essa Yacoub, Kamil Ugurbil, and Noam Harel. Reconstruction of the orientation distribution function in single-and multiple-shell q-ball imaging within constant solid angle. *Magnetic resonance in medicine*, 64(2):554–566, 2010.

[60] Martin Kochmański, Tadeusz Paszkiewicz, and Sławomir Wolski. Curie–weiss magnet—a simple model of phase transition. *European Journal of Physics*, 34(6):1555, 2013.

[61] Sacha Friedli and Yvan Velenik. *Statistical mechanics of lattice systems: a concrete mathematical introduction*. Cambridge University Press, 2017.

[62] Lev Davidovich Landau. On the theory of phase transitions. I. *Zhurnal Eksperimental'noi i Teoreticheskoi Fiziki*, 11:19, 1937.